Article

Exciton Superposition across Moiré States in a Semiconducting Moiré Superlattice

Zhen Lian[1,8], Dongxue Chen [1,8], Yuze Meng[1], Xiaotong Chen[1], Ying Su[2], Rounak Banerjee[3], Takashi Taniguchi [4], Kenji Watanabe [5], Sefaattin Tongay [3], Chuanwei Zhang [2], Yong-Tao Cui [6] ✉ & Su-Fei Shi [1,7] ✉

Moiré superlattices of semiconducting transition metal dichalcogenides enable unprecedented spatial control of electron wavefunctions, leading to emerging quantum states. The breaking of translational symmetry further introduces a new degree of freedom: high symmetry moiré sites of energy minima behaving as spatially separated quantum dots. We demonstrate the superposition between two moiré sites by constructing a trilayer WSe_2/monolayer WS_2 moiré heterojunction. The two moiré sites in the first layer WSe_2 interfacing WS_2 allow the formation of two different interlayer excitons, with the hole residing in either moiré site of the first layer WSe_2 and the electron in the third layer WSe_2. An electric field can drive the hybridization of either of the interlayer excitons with the intralayer excitons in the third WSe_2 layer, realizing the continuous tuning of interlayer exciton hopping between two moiré sites and a superposition of the two interlayer excitons, distinctively different from the natural trilayer WSe_2.

Design and control of symmetries can lead to symmetry-protected states that are promising to revolutionize the field of quantum materials. For example, breaking the inversion symmetry or time-reversal symmetry can lead to Weyl semimetals[1]. The inversion symmetry breaking in transition metal dichalcogenides (TMDCs) gives rise to a valley degree of freedom that is promising for valleytronics and quantum information science based on valley-spin[2], which can be accessed through chiral light.

The recent emergence of semiconducting TMDC superlattices[3–9], which are constructed through twisted TMDCs with a lattice mismatch or twist angle, enables spatial control of the excitons in two-dimension (2D) with the tunable periodicity of 1–10 nm and ushers in unprecedented opportunities in engineering electrons and excitons, leading to intriguing correlated electronic states[3,6,10–15], the array of quantum emitters, and correlated exciton states resulting from flat excitonic band[16–18].

Translation symmetry breaking in TMDC moiré superlattices introduces a new degree of freedom: moiré sites, the high symmetry points in a moiré supercell, which can be local energy minima and act as quantum dots[5,19,20] that can confine electrons and excitons, as schematically shown in Fig. 1c. In addition, these high symmetry points are protected by the three-fold rotation symmetry and possess the unique valley degree of freedom through the pseudo angular momentum conservation[4,19]. As a result, coupling and hybridization of these high symmetry points will usher in new venues toward quantum information storage and processing. However, unlike the energy degeneracy of different valleys (K and K'), the energy barrier between different moiré sites (on the order of 10 s' meV), along with their spatial separation, greatly suppresses the direct coupling between these moiré sites.

Here, we demonstrate the superposition between two different moiré sites by introducing a layer degree of freedom to the TMDC

[1]Department of Chemical and Biological Engineering, Rensselaer Polytechnic Institute, Troy, NY 12180, USA. [2]Department of Physics, University of Texas, Dallas, TX 75083, USA. [3]School for Engineering of Matter, Transport and Energy, Arizona State University, Tempe, AZ 85287, USA. [4]International Center for Materials Nanoarchitectonics, National Institute for Materials Science, 1-1 Namiki, Tsukuba 305-0044, Japan. [5]Research Center for Functional Materials, National Institute for Materials Science, 1-1 Namiki, Tsukuba 305-0044, Japan. [6]Department of Physics and Astronomy, University of California, Riverside, California 92521, USA. [7]Department of Electrical, Computer & Systems Engineering, Rensselaer Polytechnic Institute, Troy, NY 12180, USA. [8]These authors contributed equally: Zhen Lian, Dongxue Chen. ✉e-mail: yongtao.cui@ucr.edu; shis2@rpi.edu
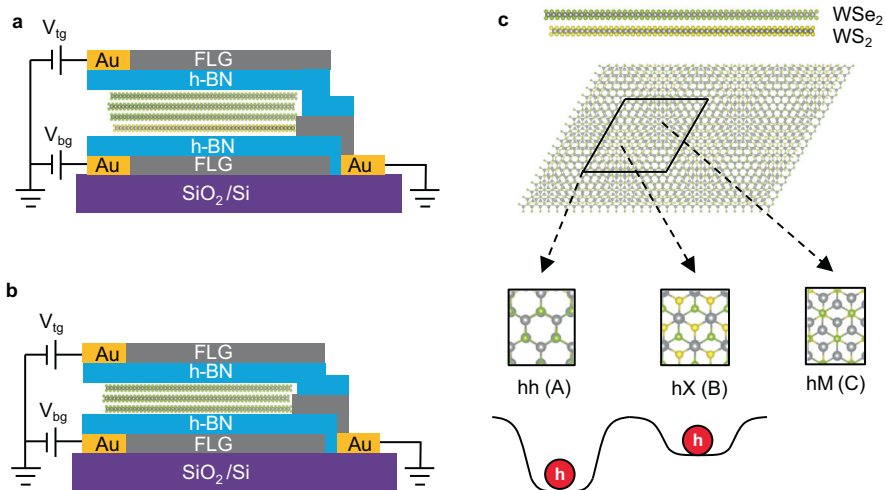
Fig. 1 | Moiré site degree of freedom. a and **b** are schematics of 3 L WSe$_2$/ 1 L WS$_2$ moiré heterojunction device and natural trilayer WSe$_2$ devices, respectively. Both devices are in a dual-gate configuration. **c** is the schematic of the WSe$_2$/WS$_2$ moiré superlattice, with three high symmetry points of C3 symmetry shown as hh, hX and hM. The naming convention of hh, hX and hM corresponds to aligning the hexagon center of the hole layer (WSe$_2$) with the hexagon center (h), the chalcogen atom (X), and the metal atom (M) of the electron layer (WS$_2$)[20], which we also call as A, B and C moiré sites for convenience. A and B sites are energy minima for holes and behave as quantum dots that confine carriers and excitons. We use the holes for illustration in **c**, but the trapping of electrons and excitons will be similar.

moiré superlattice. It is well known that the two neighboring layers of 2-H TMDC flakes, due to the intralayer inversion symmetry breaking, possess a layer degree of freedom that acts as pseudospins alternating in odd and even layers[2,21]. In an angle-aligned trilayer WSe$_2$/monolayer WS$_2$ heterojunction (3L WSe$_2$/1L WS$_2$), new types of interlayer excitons emerge, with holes residing in the first WSe$_2$ layer either trapped in moiré A or B site (Fig. 1c)[5], and electrons with the same pseudospin residing in the third WSe$_2$ layer. In particular, we find that these two interlayer excitons can hybridize through coupling with the intralayer excitons in the third WSe$_2$ layer. The resulting hybridized exciton inherits both the large oscillator strength from the intralayer excitons and the sensitive electric field dependence from the moiré interlayer excitons[7,22–24]. More interestingly, by applying an electric field, we can drive the transition between the two interlayer moiré excitons' hybridization with the intralayer exciton in the third WSe$_2$ layer, enabling the continuous tuning of hopping of the interlayer exciton from 100% at one moiré site to 100% at the other, which is otherwise suppressed. In between the transition points, we obtain an excitonic complex that is the superimposition of the interlayer excitons that are otherwise localized at moiré A and B sites.

Results and Discussions
Gate dependence of reflectance contrast
The schematic of the 3L WSe$_2$/1L WS$_2$ moiré heterojunction is shown in Fig. 1a, which is fabricated into a dual-gated device structure in which the doping and electric field can be independently controlled. We also fabricated a device of a dual-gated 2-H phase trilayer WSe$_2$ (3L WSe$_2$) (schematically shown in Fig. 1b) for the control study.

The doping-dependent optical reflectance contrast spectra of the 3L WSe$_2$/1L WS$_2$ heterojunction device are shown in Fig. 2e, which is evidently different from that of the natural trilayer (3L) WSe$_2$ device (Fig. 2f). The most pronounced resonance for the natural trilayer WSe$_2$ (Fig. 2f) is the intralayer exciton resonance X_A, which is at ~ 1.70 eV at zero doping, redshifted compared to the A exciton resonance in monolayer WSe$_2$ (-1.73 eV)[25]. X_A is redshifted linearly for both n and p doping in a symmetric fashion, with a slope of ~1.3 meV/10^{12} cm^{-2}. IX$_{3L}$ are the interlayer excitons with the hole and electron separated in the first and third WSe$_2$ layer, which have two degenerate modes as schematically shown in Fig. 2c and are named as IX$_{3L}^+$ and IX$_{3L}^-$ ("+" and "−" denote the direction of the dipole moment in the sample coordinate. The direction of the positive electric field or dipole moment is

defined as from the top gate to the back gate in 3 L WSe$_2$, and from WSe$_2$ to WS$_2$ in 3L WSe$_2$/ 1 L WS$_2$.). IX$_{3L}^{2s}$ is the 2s state of the IX$_{3L}$. The natures of IX$_{3L}$ and IX$_{3L}^{2s}$ become obvious in our later discussion of the electric field dependent reflectance contrast spectra. Zoom-in of Fig. 2f with enhanced contrast is plotted in Fig. S2 to show IX$_{3L}$ and IX$_{3L}^{2s}$ more clearly. Accompanying X_A is a less pronounced resonance X_A' with a larger slope (2.7 meV/10^{12} cm^{-2}). X_A' is likely the exciton resonance of the middle (second) layer WSe$_2$ and is not the focus of this work (see detailed discussion in Supplementary Section 14).

In the optical reflectance contrast spectra of 3L WSe$_2$/1L WS$_2$ moiré heterojunction (Fig. 2e), there is an exciton resonance (X_M^I) located at the lower energy side of X_A (-1.667 eV), which is only observable in angle-aligned 3L WSe$_2$/1L WS$_2$ heterojunctions but absent in heterojunctions with large twist angles (See supplementary section 10 for detailed discussion). X_M^I is the previously discovered moiré intralayer exciton peak in the first layer WSe$_2$ interfacing WS$_2$, with the exciton trapped at the moiré A site. The doping dependence of X_M^I clearly show the signature of the correlated insulating states at the filling factor of 1 and −1, corresponding to one electron and one hole per moiré superlattice, which was discussed in our previous publication[26]. On the p-doping side, the exciton resonances of X_A and X_A' are labeled as such due to their similar behaviors compared with that from the trilayer WSe$_2$ (Fig. 2f), with a redshift slope of 1.0 and 2.1 meV/10^{12} cm^{-2}, respectively. The n-doping side is different because the electrostatically introduced electrons are in the WS$_2$ layer instead of the WSe$_2$ layers due to the type II alignment, leaving the WSe$_2$ layers charge-neutral. We identify the X_A and X_A' in the n-doping side through their slopes as well, 1.0 and 2.1 meV/10^{12} cm^{-2}, respectively, the same as those in the p-doping region. The abrupt blueshift of the X_A in the n-doping side (starts at $n > 1$ and resonant energy around 1.725 eV) is likely due to the built-in electric field on WSe$_2$ layers arising from the electron accumulation in WS$_2$. We leave the related discussion in Supplementary Information Section 15. The focus of our work here is on the interlayer excitons within the 3L WSe$_2$ of the 3L WSe$_2$/1L WS$_2$ moiré heterojunction, with their schematics shown in Fig. 2a, b. The IX$_{3L}^+$ branch is visible and pronounced at the blue arrow in Fig. 2e, partially because it hybridizes with intralayer excitons and gains some oscillator strength but also because it retains the extended nature of interlayer excitons, hence sensing dielectric environment change associated with the Mott insulator transition at filling of one electron per moiré superlattice
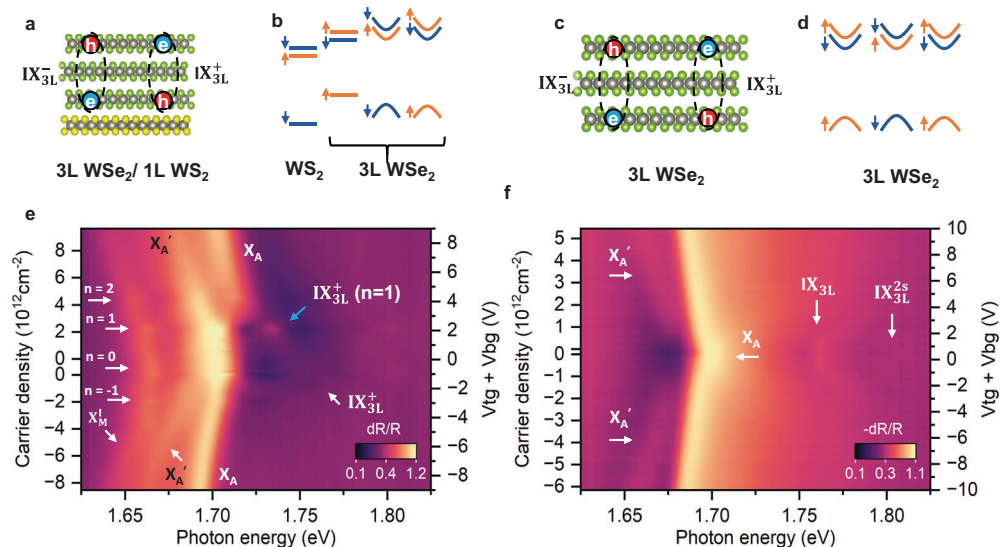
Fig. 2 | Doping-dependent reflectance contrast spectra of 3L WSe$_2$/1L WS$_2$ and natural trilayer WSe$_2$ Devices. a, **b** and **e** are the schematic atomic structure, band alignment, and the doping-dependent reflectance contrast spectra of 3L WSe$_2$/1L WS$_2$ measured from device D1. **c**, **d** and **f** are the schematic atomic structure, band alignment, and the doping-dependent reflectance contrast spectra of natural trilayer WSe$_2$ measured from device D2. The blue arrow in **e** denotes the enhanced reflection signal of the hybridized exciton (interlayer exciton IX$_{3L}^+$ hybridized with intralayer exciton) at the Mott insulator state at $n = 1$.

($n = 1$). The nature of both resonances are revealed in our later discussion of the electric field dependence study.

Interlayer hybridized excitons in 3L WSe$_2$

The electric field-dependent reflectance contrast spectra of the trilayer WSe$_2$ device is shown in Fig. 3a, which is symmetric about the electric field due to its symmetric structure. The most noticeable feature is the "cross" pattern originating from the electric field evolution from interlayer exciton IX$_{3L}$. The slope of each branch of the cross is roughly the same. These are arising from the Stark shift of the interlayer exciton IX$_{3L}$, with the two degenerate modes (IX$_{3L}^-$ and IX$_{3L}^+$) shifting oppositely under an electric field due to the dipole moment of opposite polarity. The Stark energy shift can be expressed as $\Delta E = -edF$, where F is the local electric field, e is the electron charge, and d is the electron and hole separation. We extract the value of d to be about 1.26 nm for both IX$_{3L}^-$ and IX$_{3L}^+$, which is about twice that of interlayer exciton dipole moment in WSe$_2$/WS$_2$ (0.7 nm)[7], confirming that the electron and hole of interlayer exciton occupy the two outside WSe$_2$ layers in a natural trilayer WSe$_2$.

The level avoiding at the intralayer exciton A (~1.70 eV) in Fig. 3a arises from the hybridization of the interlayer exciton and intralayer exciton. In the 2H trilayer WSe$_2$, there is significant tunneling of holes between the first and third layer WSe$_2$ as they have the same valley-layer pseudo spin, allowing the hybridization of the interlayer excitons with the intralayer excitons in either the first or third WSe$_2$ layer[27], as schematically shown in Fig. 3d. This hybridization can be well captured by a coupled two-level system, which is given by the following Hamiltonian in the basis of intralayer exciton and interlayer exciton:

$$\begin{bmatrix} X_a & \Delta \\ \Delta & X_i(F) \end{bmatrix} \qquad (1)$$

where X_a is the energy of the intralayer exciton, $X_i(F)$ is the energy of the interlayer exciton at a given electric field F, Δ is the coupling strength (see Supplementary Information Section 13 for details).

Take the positive electric field (direction defined in Fig. 3d) scenario as an example (Fig. 3c): a linearly dispersed interlayer exciton IX$_{3L}^+$ (white dotted line in Fig. 3c) and a non-dispersed intralayer exciton X$_A$ (black dotted line) can be used to well fit the observed hybridized spectra (red and blue dashed lines). From the fitting, we extract

the coupling strength to be 10.7 ± 0.3 meV, larger than the linewidth of the hybridized exciton (~9.0 ± 0.3 meV). The scenario of the negative electric field is similar, where the other interlayer exciton mode, IX$_{3L}^-$, hybridizes with the intralayer exciton (X$_A$) when the energy of the two excitons is tuned to resonance via the electric field. It is worth noting that we ignore the conduction band hybridization of the first and third layer WSe$_2$, which is theoretically predicted to be nonzero but orders of magnitude smaller than the holes[27]. The neglection of the conduction band hybridization is also justified by the electric-field-dependent reflectance contrast spectra of 3L WSe$_2$/1L WS$_2$, which is asymmetric about positive and negative electric fields (later discussion of Fig. 4).

The additional level avoiding at the energy around 1.79 eV in Fig. 3a is due to the hybridization of the interlayer exciton (IX$_{3L}$) with the 2s state of intralayer A exciton (Fig. 3a and Fig. S4a, b). The second level avoiding at higher energy (~1.80 eV) is due to the hybridization of the excited state of the interlayer exciton (IX$_{3L}^{2s}$) and 2s of the A exciton, which we enhance the contrast and show in Fig. S4a, b. It is interesting to note that the energy difference between the ground state and 2s of interlayer exciton IX$_{3L}$ is about 51 meV, smaller but at the same order of magnitude compared with the energy difference between 2s and 1s of A exciton for trilayer WSe$_2$ (~95 meV, Fig. S4a, b), suggesting the strongly bound nature of the interlayer exciton IX$_{3L}$. All these hybridization features are absent in a dual-gated nature bilayer WSe$_2$ (Fig. S8), which is AB stacked with two layers of different layer pseudospin, further confirming our interpretation. The electric-field-dependent reflectance contrast spectra of a 4L WSe$_2$ device (Fig. S7) show similar hybridization features but with two "crosses" slightly shifted in energy, about 10 meV. According to the interpretation of the 3L WSe$_2$ data, these two crosses are the two types of interlayer excitons from the 1st and 3rd layer WSe$_2$ and the 2nd and 4th layer WSe$_2$, which slightly shift in energy due to possible dielectric environment differences[28,29].

Hybridized Excitons across Moiré States in 3L WSe$_2$/1L WS$_2$

We now turn to the study of the electric field-dependent reflectance contrast spectra of the 3L WSe$_2$/1L WS$_2$ moiré heterojunction, shown in Fig. 4c. The negative electric field side has some similarity compared with that from trilayer WSe$_2$, while the positive electric field side is significantly different. More specifically, the hybridized spectrum on the positive electric field side involves three exciton branches: two
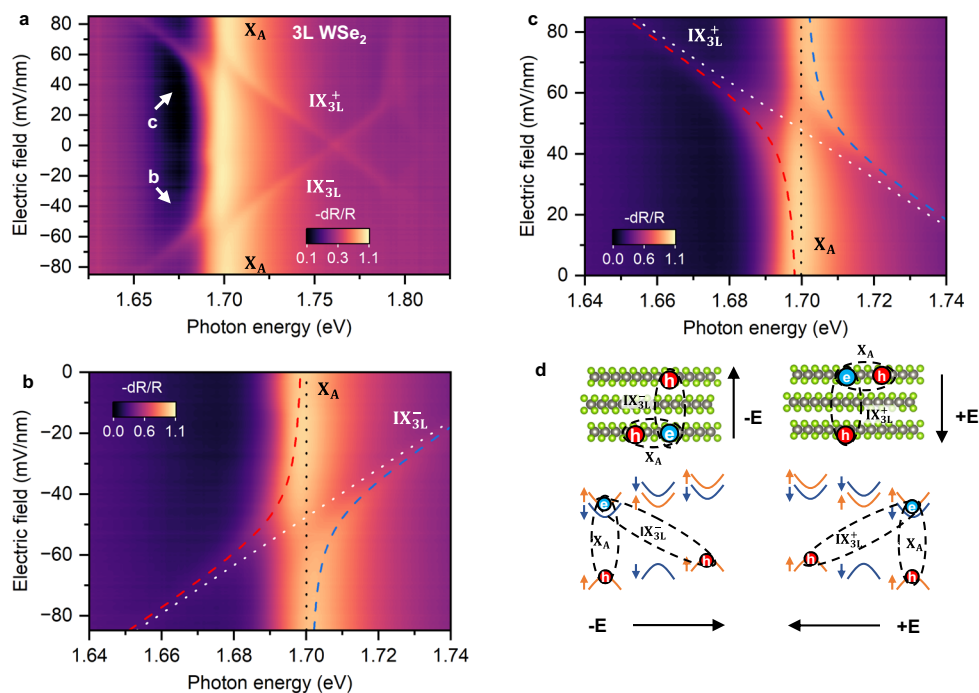
Fig. 3 | Interlayer and intralayer exciton hybridization in natural trilayer WSe$_2$. **a** shows the electric field dependence of reflectance contrast spectra measured from natural trilayer WSe$_2$ device (D2) plotted in log scale. **b** is the zoom-in of **a** in the region between 1.64 eV and 1.74 eV at negative electric fields plotted in linear scale. **c** is the zoom-in of **a** in the region between 1.64 eV and 1.74 eV at positive electric fields plotted in linear scale. The dashed red and blue lines show the fitting result of the hybridized excitonic states obtained by fitting the peak positions with a two-level hybridization model. The white and black dotted lines are the energies of unhybridized intralayer and interlayer excitons obtained from the fitting. **d** shows the schematics of the interlayer and intralayer excitons involved in the hybridization, both in real space and the band alignment configurations.

dispersive (white dotted lines in Fig. 4e) and one non-dispersive (black dotted line in Fig. 4e) branch. The necessity of involving three exciton branches is also obvious from the derivative of Fig. 4e with respect to the electric field, as shown in Fig. S3d. The two dispersive excitons have a similar slope for the Stark shift, translating to electron and hole separations of 1.313 ± 0.004 nm and 1.609 ± 0.004 nm (fitting details in Supplementary Information Section 13). Therefore, they are the interlayer excitons, similar to IX_{3L}^{+} in the natural trilayer WSe$_2$, with the hole in the first WSe$_2$ layer interfacing WS$_2$ and the electron in the third WSe$_2$ layer away from the interface. The two different interlayer excitons stem from the moiré coupling modified valence band of the first WSe$_2$ layer. As schematically shown in Fig. 4a and b, the moiré modulation folds the valence band of the first WSe$_2$ layer into moiré minibands. The two interlayer excitons correspond to holes occupying the two moiré minibands located at different moiré sites[20], which effectively behave as two spatially separated quantum dots. Each of them is located at an energy minimum at a high symmetry point within the moiré unit cell, which we call moiré A and B sites, respectively. We thus label these two interlayer excitons as $IX_{3L}^{+\,(A)}$ and $IX_{3L}^{+\,(B)}$. Since the WS$_2$ and first WSe$_2$ layer are aligned at 60 degrees (H stacked) as determined by the second harmonic generation (SHG) spectra (Fig. S5), the moiré A and B sites correspond to the H_h^h and H_h^X stacking configurations shown in Fig. 4b. The energy separation of the two interlayer excitons at zero electric field, 69 meV, represents the energy difference between the top two moiré minibands, if we ignore the difference in exciton binding energy. This value is consistent with the energy difference between the intralayer excitons trapped at moiré A and B sites in the WSe$_2$/WS$_2$ moiré superlattice, ~53 meV[26]. The remaining non-dispersive branch corresponds to the intralayer exciton, X$_A$, with both hole and electron in the third WSe$_2$ layer. Therefore, $IX_{3L}^{+\,(A)}$, $IX_{3L}^{+\,(B)}$, and X$_A$ hybridize by sharing the electron in the third WSe$_2$ layer. The above picture of hybridization involving two moiré interlayer excitons are confirmed by a control device (D4) of 3 L WSe$_2$/

1 L WS$_2$ in the dual-gate configuration, with an intentionally misaligned angle (20-degree) between WSe$_2$ and WS$_2$ layers. The electric-field-dependent reflectance contrast spectra (Fig. S11) indeed become symmetric about the electric field and similar to that of natural 3 L WSe$_2$, and they show no signs of interlayer moiré excitons ($IX_{3L}^{+\,(A)}$ and $IX_{3L}^{+\,(B)}$).

It is worth noting that direct tunneling between moiré A and B sites is suppressed due to the energy barrier, their spatial separation, and different stacking symmetry. Therefore, a direct hybridization between these two sites is difficult to achieve, unlike the degenerate valley-spin bands in TMDCs. However, with the assistance from the mobile intralayer exciton in the third WSe$_2$ layer, hybridization of moiré A and B sites is realized, and we can controllably tune the interlayer excitons IX_{3L}^{+} between moiré A and B sites. In fact, the hybridized exciton notated with the cyan dashed line is a mixture of interlayer excitons localized at the moiré A site and B site, with the probability tunable from 100% at A to 100% at B site by controlling the electric field (Fig. 4f).

On the negative electric field side, the interlayer exciton involved in the hybridization is IX_{3L}^{-}, with the hole in the third layer WSe$_2$ not experiencing the moiré modulation. Meanwhile, the intralayer exciton in the 1st WSe$_2$ layer is modified by the moiré potential to have a lower energy of ~1.667 eV and is trapped at the moiré A site, which is labeled as X_M^I. As a result, hybridization occurs between IX_{3L}^{-} and X_M^I. Their coupling strength is extracted to be 11.4 ± 0.1 meV. The interlayer exciton IX_{3L}^{-} can also couple to the other moiré excitons from the 1st layer WSe$_2$, which contributes to the weak features in Fig. 4 and are shown with enhanced contrast in Fig. S4c, d.

The asymmetry of Fig. 4c between the n- and p-doping sides further justifies our neglection of conduction band hybridization: IX_{3L}^{-} near hybridization region d in Fig. 4c goes directly through X$_A$, and IX_{3L}^{-} near region e goes directly through X_M^I, with neither showing level avoiding. If the conduction band hybridization is significant, we should
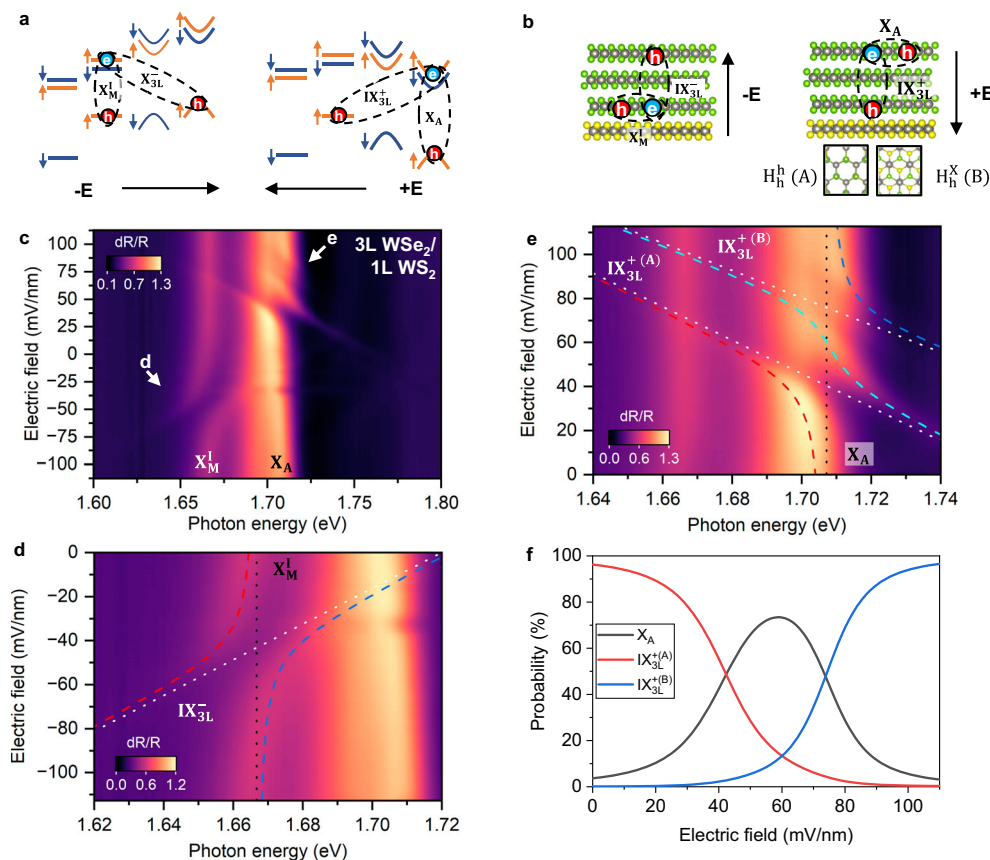
Fig. 4 | Interlayer and intralayer exciton hybridization in the angle-aligned 3L WSe₂/1L WS₂ heterostructure. **a** and **b** show the schematic band alignment and the real-space distribution of the hybridized excitons in 3L WSe₂/1L WS₂ moiré heterojunction. **c** shows the electric field dependence of reflectance contrast spectra measured from 3 L WSe₂/1L WS₂ device (D1). **d** is the zoom-in of **a** in the region between 1.62 eV and 1.72 eV at negative electric fields. **e** is the zoom-in of **a** in the region between 1.64 eV and 1.74 eV at positive electric fields. The dashed lines show the hybridized excitonic states obtained by fitting the peak positions. The dotted lines are the energies of unhybridized intralayer and interlayer excitons obtained from the fitting. A two-level hybridization model using one intralayer exciton and one interlayer exciton as bases is used to fit the peak positions in **d**, while a three-level hybridization model with one intralayer exciton and two different interlayer excitons is used to fit the peak positions in **e**. **f** shows the fractional composition of the hybridized exciton corresponding to the cyan line as a function of the electric field, expressed as the probability of each interlayer or intralayer exciton.

observe the hybridization of two interlayer excitons (due to moiré modulated conduction bands) and X_A. Similarly, the interlayer exciton from region e (IX_{3L}^+) in Fig. 4c should hybridize with X_M^I. We include a detailed discussion in Supplementary Information Section 16.

In summary, we have demonstrated a strategy to realize continuous tuning of interlayer exciton hopping between different moiré sites in 3 L WSe₂/ 1 L WS₂ moiré superlattices. These additional degrees of freedom enable the formation of a tunable honeycomb lattice of excitons with exciting opportunities for engineering new quantum states. For example, considering the large spin-orbit coupling in TMDCs, the continuous tuning of the hopping can be potentially exploited for constructing Dirac and Weyl modes of excitons, as well as the topologically protected edge states connecting these modes[19]. Our demonstration of the superposition of excitons across the different moiré sites also inspires new venues of quantum information processing and harnessing the new moiré site degree of freedom for twistronics.

Methods
Sample Fabrication
We used the same dry pick-up method[30] as reported in our earlier work to fabricate TMDC heterostructures[17,26]. The gold electrodes are pre-patterned on the Si/SiO₂ substrate. The monolayer TMDC flakes, BN flakes, and few-layer graphene (FLG) flakes are exfoliated on silicon chips with 285 nm thermal oxide. The thickness of BN flakes was determined by atomic force microscopy (AFM). The layer numbers of

WSe₂ flakes were identified by optical contrast with the assistance of second-harmonic generation (SHG). Top BN and bottom flakes with equal thickness were intentionally used for devices D1, D2, and D3. The polycarbonate (PC)/ polydimethylsiloxane (PDMS) stamp was used to pick up TMDC monolayer and other flakes sequentially. The alignment of each layer is achieved under a home-built microscope transfer stage with the rotation controlled with an accuracy of 0.02 degrees. The PC is then removed in the chloroform/isopropanol sequence and dried with nitrogen gas. The final constructed devices were annealed in a vacuum (<10⁻⁶ torr) at 250 °C for 8 hours.

Optical Measurements
During the optical measurements, a home-built confocal imaging system was used to focus the laser onto the sample (with a beam spot diameter ~ 2 μm) and collect the optical signal into a spectrometer (Princeton Instruments). The reflectance contrast measurement was performed using a supercontinuum laser source (YSL photonics). A relative flat reflectance background R_0 was obtained by fitting the reflectance spectrum at high hole-doping level with a polynomial function for each measured spot (see Supplementary Section 11 for details). The reflectance contrast is defined as $\frac{dR}{R} = \frac{R-R_0}{R_0}$. The reflectance contrast from device D1 and D2 are added by 0.3 and −0.3 for better presentation in the log scale. All optical spectroscopy measurements were performed at the temperature of 10 K with a Montana cryostat. The polarized SHG measurements were performed with a

pulsed laser excitation centered at 900 nm (Ti: Sapphire; Coherent Chameleon) with a repetition rate of 80 MHz and a power of 80 mW. The crystal axes of the sample were fixed. A half-waveplate was placed between the beam splitter and the objective and was rotated to change the polarization angles of both the excitation laser and the SHG signal.

Doping and Electric Field Calculations

The density of carriers introduced by the electrostatic gating is given by $n_e(n_p) = C_{tg}(V_{tg} - V_{tg}^0) + C_{bg}(V_{bg} - V_{bg}^0)$, where $C_{tg}(C_{bg})$ are the geometry capacitance of the top gate (back gate) and V_{tg} (V_{bg}) are the top gate (back gate) voltage. V_{tg}^0 and V_{bg}^0 are the onset gate voltages of the top gate and the back gate, determined experimentally from the regions where the 2s peaks remain visible. The electrical field in the TMDC is given by $F = \varepsilon_{BN}/\varepsilon_{TMDC}(V_{tg}/2d_1 - V_{bg}/2d_2)$, where $d_1(d_2)$ is the thickness of the top (bottom) BN determined by atomic force microscopy, $\varepsilon_{BN} = 3.5$ and $\varepsilon_{TMDC} = 7.2$ are the relative dielectric constants of h-BN and TMDC, respectively[31,32].

Data availability

The data in Figs. 1–4 are provided in the source data files. All other data that support the plots within this paper and other findings of this study are available from the corresponding author upon reasonable request. Source data are provided with this paper.

References

1. Armitage, N. P., Mele, E. J. & Vishwanath, A. Weyl and Dirac semi-metals in three-dimensional solids. *Rev. Mod. Phys.* **90**, 15001 (2018).
2. Xu, X., Yao, W., Xiao, D. & Heinz, T. F. Spin and pseudospins in layered transition metal dichalcogenides. *Nat. Phys.* **10**, 343–350 (2014).
3. Regan, E. C. et al. Mott and generalized Wigner crystal states in WSe₂/WS₂ moiré superlattices. *Nature* **579**, 359–363 (2020).
4. Jin, C. et al. Identification of spin, valley and moiré quasi-angular momentum of interlayer excitons. *Nat. Phys.* **15**, 1140–1144 (2019).
5. Jin, C. et al. Observation of moiré excitons in WSe₂/WS₂ hetero-structure superlattices. *Nature* **567**, 76–80 (2019).
6. Tang, Y. et al. Simulation of Hubbard model physics in WSe₂/WS₂ moiré superlattices. *Nature* **579**, 353–358 (2020).
7. Tang, Y. et al. Tuning layer-hybridized moiré excitons by the quantum-confined Stark effect. *Nat. Nanotechnol.* **16**, 52–57 (2021).
8. Seyler, K. L. et al. Signatures of moiré-trapped valley excitons in MoSe₂/WSe₂ heterobilayers. *Nature* **567**, 66–70 (2019).
9. Tran, K. et al. Evidence for moiré excitons in van der Waals het-erostructures. *Nature* **567**, 71–75 (2019).
10. Jin, C. et al. Stripe phases in WSe₂/WS₂ moiré superlattices. *Nat. Mater.* **20**, 940–944 (2021).
11. Xu, Y. et al. Correlated insulating states at fractional fillings of moiré superlattices. *Nature* **587**, 214–218 (2020).
12. Huang, X. et al. Correlated insulating states at fractional fillings of the WS₂/WSe₂ moiré lattice. *Nat. Phys.* **17**, 715–719 (2021).
13. Li, H. et al. Imaging moiré flat bands in three-dimensional recon-structed WSe₂/WS₂ superlattices. *Nat. Mater.* **20**, 945–950 (2021).
14. Ghiotto, A. et al. Quantum criticality in twisted transition metal dichalcogenides. *Nature* **597**, 345–349 (2021).
15. Wang, L. et al. Correlated electronic phases in twisted bilayer transition metal dichalcogenides. *Nat. Mater.* **19**, 861–866 (2020).
16. Gu, J. et al. Dipolar excitonic insulator in a moiré lattice. *Nat. Phys.* **18**, 395–400 (2022).
17. Chen, D. et al. Excitonic insulator in a heterojunction moiré super-lattice. *Nat. Phys.* **18**, 1171–1176 (2022).
18. Zhang, Z. et al. Correlated interlayer exciton insulator in hetero-structures of monolayer WSe₂ and moiré WS₂/WSe₂. *Nat. Phys.* **18**, 1214–1220 (2022).
19. Yu, H., Liu, G., Tang, J., Xu, X. & Yao, W. Moiré excitons: From pro-grammable quantum emitter arrays to spin-orbit–coupled artificial lattices. *Sci. Adv.* **3**, e1701696 (2017).
20. Naik, M. H. et al. Intralayer charge-transfer moiré excitons in van der Waals superlattices. *Nature* **609**, 52–57 (2022).
21. Jones, A. M. et al. Spin–layer locking effects in optical orientation of exciton spin in bilayer WSe₂. *Nat. Phys.* **10**, 130–134 (2014).
22. Alexeev, E. M. et al. Resonantly hybridized excitons in moiré superlattices in van der Waals heterostructures. *Nature* **567**, 81–86 (2019).
23. Leisgang, N. et al. Giant Stark splitting of an exciton in bilayer MoS₂. *Nat. Nanotechnol.* **15**, 901–907 (2020).
24. Ruiz-Tijerina, D. A. & Fal'Ko, V. I. Interlayer hybridization and moiré superlattice minibands for electrons and excitons in heterobilayers of transition-metal dichalcogenides. *Phys. Rev. B* **99**, 125424 (2019).
25. Wang, T. et al. Giant valley-polarized Rydberg excitons in mono-layer WSe₂ revealed by magneto-photocurrent spectroscopy. *Nano Lett.* **20**, 7635–7641 (2020).
26. Chen, D. et al. Tuning moiré excitons and correlated electronic states through layer degree of freedom. *Nat. Commun.* **13**, 4810 (2022).
27. Hagel, J. et al. Exciton landscape in van der Waals heterostructures. *Phys. Rev. Res.* **3**, 1–14 (2021).
28. Zhang, Y. et al. Every-other-layer dipolar excitons in a spin-valley locked superlattice. *Nat. Nanotechnol.* **18**, 501–506 (2023).
29. Feng, S. et al. Highly tunable ground and excited state excitonic dipoles in multilayer 2H-MoSe₂. https://doi.org/10.48550/ARXIV.2212.14338 (2022).
30. Wang, L. et al. One-dimensional electrical contact to a two-dimensional material. *Science* **342**, 614–617 (2013).
31. Laturia, A., Van de Put, M. L. & Vandenberghe, W. G. Dielectric properties of hexagonal boron nitride and transition metal dichal-cogenides: from monolayer to bulk. *npj 2D Mater. Appl.* **2**, 6 (2018).
32. Kim, K. et al. Band alignment in WSe₂-graphene heterostructures. *ACS Nano* **9**, 4527–4532 (2015).

Author contributions

S.-F.S. conceived the project. Z.L., D.C. and Y.M. fabricated devices. Z.L. performed measurements. M.B. and S.T. grew the TMDC crystals. T.T. and K.W. grew the BN crystals. S.-F. S., Y.-T.C., Z.L. and D.C. analyzed the data. S.-F. S. supervised the project. S.-F. S. and Y.-T. C. wrote the manuscript with input from all authors.

Competing interests

The authors declare no competing interest.

Additional information

Supplementary information The online version contains supplementary material available at
https://doi.org/10.1038/s41467-023-40783-z.

Correspondence and requests for materials should be addressed to Yong-Tao Cui or Su-Fei Shi.

Peer review information *Nature Communications* thanks Nadine Leisgang, and the other, anonymous, reviewer(s) for their contribution to the peer review of this work. A peer review file is available.

Reprints and permissions information is available at http://www.nature.com/reprints

Publisher's note Springer Nature remains neutral with regard to jurisdictional claims in published maps and institutional affiliations.